Nanoscale Rheology and Anisotropic Diffusion Using Single Gold Nanorod Probes

Mehdi Molaei, Ehsan Atefi, and John C. Crocker*
Chemical and Biomolecular Engineering, University of Pennsylvania, 220 South 33rd Street, Philadelphia, Pennsylvania 19104, USA

(Received 30 September 2017; revised manuscript received 4 January 2018; published 15 March 2018)

The complex rotational and translational Brownian motion of anisotropic particles depends on their shape and the viscoelasticity of their surroundings. Because of their strong optical scattering and chemical versatility, gold nanorods would seem to provide the ultimate probes of rheology at the nanoscale, but the suitably accurate orientational tracking required to compute rheology has not been demonstrated. Here we image single gold nanorods with a laser-illuminated dark-field microscope and use optical polarization to determine their three-dimensional orientation to better than one degree. We convert the rotational diffusion of single nanorods in viscoelastic polyethylene glycol solutions to rheology and obtain excellent agreement with bulk measurements. Extensions of earlier models of anisotropic translational diffusion to three dimensions and viscoelastic fluids give excellent agreement with the observed motion of single nanorods. We find that nanorod tracking provides a uniquely capable approach to microrheology and provides a powerful tool for probing nanoscale dynamics and structure in a range of soft materials.

DOI: 10.1103/PhysRevLett.120.118002

The Brownian motion of embedded tracers has been applied to determining the viscoelasticity of soft materials and microscopic objects via passive microrheology for more than two decades. Typically, dynamic light scattering [1–4] or image-based particle tracking [3,5–9] is used to measure the tracers' mean-squared displacement (MSD), which is then converted to the dynamic shear modulus via a generalized Stoke-Einstein relation (GSER) [1,2,4,10]. Pioneering work by Cheng and Mason [11] showed that the rotational diffusion of anisotropic micron-scale particles can also be used to quantify the rheology via a rotational GSER, and later it was demonstrated using depolarized dynamic light scattering [12,13]. Multiple imaging-based rotational tracking methods have since been reported [14–18]; however, they do not appear well suited to microrheology. While the use of anisotropic nanoparticle tracers would greatly facilitate the application of this approach to stiffer materials and much smaller length and time scales than possible with larger tracers, microrheology places stringent requirements on the accuracy of the tracer's inferred mean-squared displacement. Indeed, despite several reports of gold nanorod (GNR) rotational tracking using imaging [19–31] and depolarized scattering [32–36], no one has demonstrated the use of GNRs to accurately measure the rheology of a viscoelastic material. Moreover, no models of the complex anisotropic translational diffusion [32,33,37] that these particles would execute in a viscoelastic material, or its coupling to the rotational diffusion, have been reported or validated.

Here, we study the rotational and translational Brownian motion of single GNRs using a laser-illuminated dark-field microscope modified to simultaneously record two orthogonally polarized images. A polarimetric analysis, based upon a nano-optical model of the GNR, enables the accurate determination of the rods' three-dimensional orientation to better than one degree at up to several thousand frames per second. The rotational diffusion motion quantified by a mean-squared angular displacement can be quantitatively converted into a dynamic shear modulus via a generalized Stokes-Einstein relation. We demonstrate this "nanorheology" approach in concentrated viscoelastic solutions of polyethylene glycol polymer, extending passive microrheology down to 100 nm length and single attoliter (10^{-18} l) volume scales. Moreover, we extend an earlier study [37] of two-dimensional anisotropic translational diffusion [38] in Newtonian fluids to the unbounded, three-dimensional and the viscoelastic cases and find that it accurately reproduces the observed motion of single isolated nanorods.

GNRs are ideal orientation probes, since their surface plasmon resonance [22] depends on their relative orientation with respect to the external electric field [39] and their scattered light is thus strongly polarized [26,40]. Previous studies [26,39,40] have shown that far-field scattered light of a single GNR can be modeled by the electric field emitted from three independent and orthogonal principal dipoles, with the dipole aligned along the rod's long axis being predominant. We computed the strength of these principal dipoles using the discrete dipole approximation method [41–44] (see Supplemental Material Sec. I.1 for details [45]). We image the particles using a custom-built dark-field microscope that focuses a single mode, 300 mW diode pumped solid state laser ($\lambda = 670$ nm) in the back aperture of a high-NA, oil-immersion objective to produce

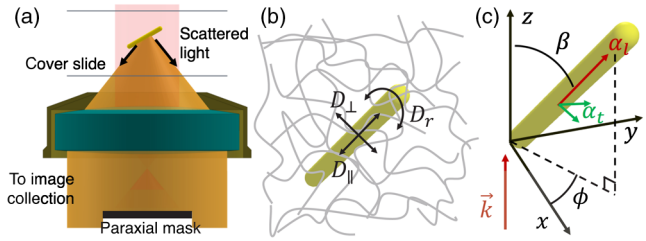

FIG. 1. (a) GNR scattering and imaged by a dark-field microscope. (b) GNR embedded in viscoelastic polymer solution. (c) Coordinate system of the GNR defined by polar β and azimuthal angles φ.

a small, collimated Gaussian beam in the specimen [Fig. 1(a)]. We took advantage of the polarization sensitivity of GNR scattering by illuminating the rod with a circularly polarized laser beam and splitting the scattered light into two images on the same camera detector, corresponding to two orthogonal linear polarization channels [45]. The integrated intensity of the GNR images in these two channels is a function of the GNR orientation, specifically, its polar angle β and azimuthal angle φ [Fig. 1(c)]. We use a semianalytic physical optics model to compute the expected intensities in our high-numerical-aperture microscope. Inverting these periodic functions maps the inferred position of the rod's orientation into a single octant domain of the unit sphere. While this precludes determining the absolute spatial orientation of the rod, it does allow the angular mean-squared displacement, needed for microrheology, to be reliably determined.

To demonstrate the angular tracking capability of the imaging system, we first studied the motion of GNRs (20×100 nm^2) in pure glycerol. The intensity of the scattering light in the x and y channels and the total intensity are shown as functions of the time in Figs. 2(a) and 2(b). Figure 2(c) shows the inferred polar and azimuthal angles of a single GNR versus the time. As expected, the inferred GNR orientation, as shown in Fig. 2(d), fully explores the available octant of a unit sphere. Typical images of the GNR at different orientations at selected times are shown in Fig. 2(f). Tracking the centroid position of the GNR over time [Fig. 2(g)] indicates that translational Brownian motion of the GNR is small enough that rods do not go out of focus during image collection. The shape of the distribution of polar angles and azimuthal angles over 10^5 image pairs is consistent with the GNR exploring all orientations randomly to within statistical sampling [Fig. 2(h)], confirming the accuracy of our polarimetric analysis [46–52].

The mean-squared angular displacement (MSAD), $\mathrm{MSAD} = \langle |u(t+\tau) - u(t)|^2 \rangle_t$, is bounded by the direction vector being limited to the unit sphere, leading to a single exponential crossover with an asymptote of 2, $\langle -\Delta\hat{u}^2(t) \rangle = 2[1-(1-\varepsilon_r^2)\exp(-2D_r t)]$, where D_r is the rotational diffusion coefficient and ε_r is the measurement error in

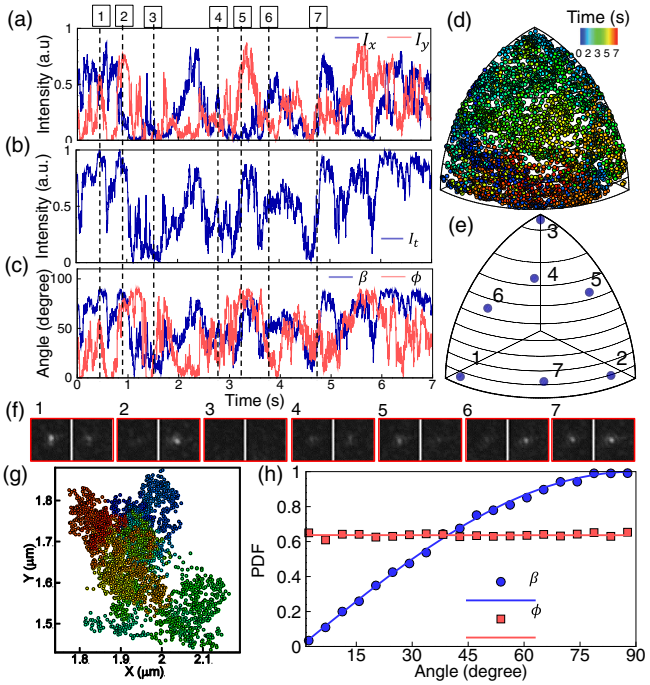

FIG. 2. Integrated intensity of a GNR in glycerol in orthogonal x and y polarization images (a), with the corresponding sum of intensities (b) and the inferred orientation angles (c). Time-dependent 3D GNR orientation mapped into a single octant (d). Orientations of selected time points (1–7) marked in (e), corresponding image pairs (1.6×1.6 μm^2) in (f). Trajectory (g) of the GNR showing translational motion. Frequency distributions of orientation angles (h) from 10^5 image pairs (symbols) match a random orientation model (curves).

the orientation vector [14,53,54] [Fig. S5(a)]. With unit vectors mapped to an octant, a similar effect occurs; Monte Carlo (MC) simulations [45] show that the resulting MSAD is well described empirically by a stretched exponential function with an asymptote of 0.5:

$$\langle |\Delta\hat{u}^2(t)| \rangle = \frac{1}{2}\{1-(1-\varepsilon_r^2)\exp[-(\kappa D_r t)^\zeta]\}, \quad (1)$$

where $\kappa = 1.6$ and $\zeta = 0.95$ are constants [Fig. 3(a)]. Equation (1) compares favorably to the MSAD determined for single GNRs in pure glycerol [Fig. 3(b)]. Fitting yields a rotational diffusion constant $D_r = 3.5$ rad^2/s and an estimated angular measurement uncertainty $\varepsilon_r^2 = 2.5 \times 10^{-4}$ rad^2, better than 1° directional precision. We also determined the translational diffusion coefficient by fitting to the short lag time data from centroid-based particle tracking [53] [Fig. S5(c)]: $\langle \Delta r_{xy}^2 \rangle = 4D_t t + 4\varepsilon_t^2$. This yields a value of $D_t = 0.007$ μm^2/s and a position uncertainty of ~9 nm.

The theoretical prediction of translational and rotational diffusion coefficients for a rod (in the lab frame) are $D_r = [(3KT)/(\pi\eta l^3)][\ln\rho + C_r(\rho)]$ and $D_t = [(KT)/(3\pi\eta l)]$

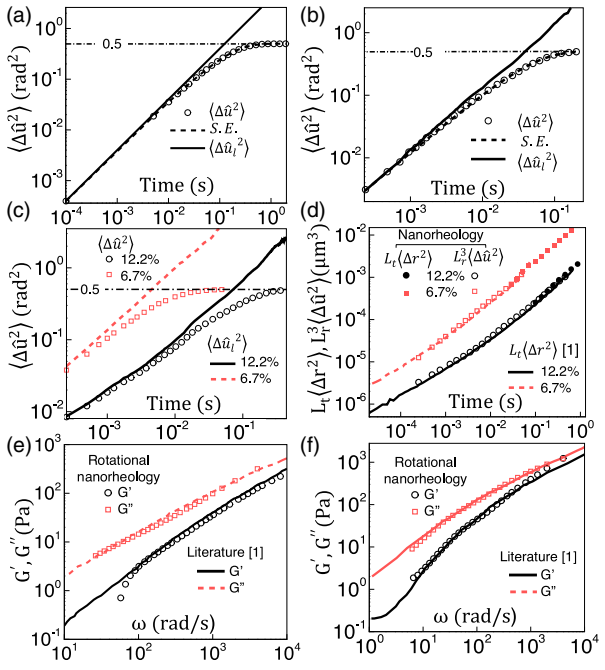

FIG. 3. MSADs of simulated (a) and measured (b) GNR in glycerol (circles), stretched exponential fit (dashed line), and unbounded MSAD (curve). Measured MSADs (c) of a GNR in 200 kDa PEO, 6.7% w/w (squares) and 12.2% w/w (circles). (d) Scaled unbound MSAD (open symbols), translational MSD (closed circles) of the GNR, and rescaled microsphere MSD [1] (lines) at two PEO concentrations. Storage and loss moduli for the PEO solution obtained from GNR rotational nanorheology (symbols) and literature microrheology [1] (lines) at 6.7% w/w (e) and 12.2% w/w (f).

$[\ln\rho + C_t(\rho)]$, where K and T are the Boltzmann constant and temperature, respectively, l and d are the length and diameter, respectively, of the rod, and C_r and C_t are, respectively, the rotational and translational drag coefficient correction factors which are a function of the aspect ratio ρ and the shape of the rod ends [18,55,56]. The ratio of the translational to the rotational diffusion coefficients is only a function of the geometry of the GNR: $(D_t/D_r) = l^2 f(\rho)$. Electron microscopy shows that the rods have a consistent 20 nm diameter and lengths of 100 ± 11 nm; data are shown in Supplemental Material [45]. Using a spherocylinder model and assuming the rods are stripped of their CTAB ligands in neat glycerol, the length of the single GNR tracer is inferred to be $l = 107 \pm 2$ nm, and the viscosity of the solution can be estimated as $\eta = 1.26$ Pa s, in excellent agreement with the expected value of 1.29 Pa s, for pure glycerol at 21 ± 1.5 °C.

The rotational diffusion of a nanorod in a viscoelastic material has been described by a Langevin torque equation $I_r\dot{\Omega}(t) = \Gamma_r(t) - \int_0^t \tilde{\xi}_r(t-\tau)\Omega(\tau)d\tau$, where Ω is the angular velocity of the nanorod, Γ_r is the thermal driving torque, and $\tilde{\xi}_r$ is the rotational memory function [11]. Mason *et al.* have shown that the solution of this equation is similar to that for the translational Langevin equation [3]. Taking the Laplace transform of the Langevin equation, applying the principles of causality and thermal energy equipartition, and neglecting the inertia term, the Laplace transform of the angular velocity will be $\langle\tilde{v}(0)\tilde{v}(s)\rangle = k_BT/\tilde{\xi}_r(s)$. Taking the GNR as a spherocylinder leads to the Laplace transform of the rotational memory function to be $\tilde{\xi}_r(s) = \frac{1}{3}\pi l^3\tilde{\eta}(s)/[\ln(\rho) + C_r]$, where $\tilde{\eta}(s)$ is the frequency-dependent viscosity. Replacing $\langle\tilde{v}(0)\tilde{v}(s)\rangle$ with $(s^2/2)\langle\Delta\tilde{u}_l^2(s)\rangle$ leads to the rotational generalized Stokes-Einstein relation (RGSER) for the GNR

$$\tilde{G}(s) = s\tilde{\eta}(s) = \frac{6k_BT}{\pi s l^3\langle\Delta\tilde{u}_l^2(s)\rangle}[\ln\rho + C_r], \qquad (2)$$

where $\Delta\tilde{u}_l^2(s)$ is the Laplace transform of an MSAD, $\langle\Delta\hat{u}_l^2(t)\rangle$, that unlike $\langle\Delta\hat{u}^2(t)\rangle$ is unbounded in magnitude at a long lag time. We developed an approach that computes a lag-time-independent mapping between these two bounded and unbounded MSADs by inverting Eq. (1), which leads to $\langle\Delta\hat{u}_l^2(t)\rangle = 4D_rt = (4/k)\{\ln[1/(1-2\langle\Delta\hat{u}^2(t)\rangle)]\}^{1/\zeta}$. We validated this procedure using simulated trajectories of tracer beads in different model viscoelastic fluids using a method developed by Khan and Mason [50]; see Supplemental Material Sec. I.7 [45]. This procedure has the expected effect of linearizing the bounded MSAD of GNR in the glycerol solution; see Fig. 3(b). A limitation of this approach is the amplification of uncertainties in $\langle\Delta\hat{u}^2(t)\rangle$ for lag times longer than the rod's Brownian tumbling time, which limits the usefulness of this method as the bounded MSAD approaches its asymptotic values.

To demonstrate the feasibility of using Eq. (2) to measure nondiffusive Brownian motion and viscoelasticity with single GNRs, we suspended rods in an aqueous polyethylene oxide (PEO) solution (200 K molecular weight, 6.7% and 12.2% w/w), previously employed in a microrheology study by Dasgupta *et al.* [1]. In both samples, the diameter of the rods is larger than the mesh sizes of the entangled polymer solutions at these concentrations (see Supplemental Material for more details of the polymer characteristics [45]). Measured bounded MSADs, shown by symbols in Fig. 3(c), were remapped to unbounded MSADs, shown in Fig. 3(c) by lines.

To validate our tracking results, we can compare them to those of the earlier microsphere study using the same viscoelastic sample, by rescaling the MSDs as $L_t\langle\Delta\tilde{r}^2(s)\rangle$ and MSADs with $L_r^3\langle\Delta\tilde{u}_l^2(s)\rangle$, where L_t and L_r are, respectively, the translational and rotational effective length of probes derived from equating $\tilde{G}(s) = s\tilde{\eta}(s) = [(2k_BT)/(\pi sL_r^3\langle\Delta\tilde{u}_l^2(s)\rangle)] = [(2k_BT)/(\pi sL_t\langle\Delta\tilde{r}^2(s)\rangle)]$. For a sphere of diameter d, $L_t = L_r = d$, and for a nanorod with a length of l and an aspect ratio of ρ, $L_t = [l/(\ln\rho + C_t)]$ and $L_r = [l/(\sqrt[3]{\ln\rho + C_r})]$. The $L_r^3\langle\Delta\hat{u}_l^2\rangle$ and $L_t\langle\Delta r^2\rangle$ of our single GNRs in the two PEO solutions is shown with open

and closed symbols, respectively, in Fig. 3(d). As in glycerol, the length of the GNRs in the 6.7% and 12.2% w/w PEO solution samples are determined by aligning the scaled MSDs and MSADs of the GNRs to be $l = 94 \pm 2$ nm in the 6.7% sample and $l = 101 \pm 2$ nm in 12.2%, respectively. Our results compare favorably with $L_t\langle\Delta r^2\rangle$ of 0.65 μm diameter microspheres, deduced from the previous microrheology study [1] differing systematically by about 15%. Because excess CTAB was added to the PEO solution, we assume that the CTAB layers are intact and that the effective rod diameter, 26 nm, is correspondingly larger than seen using EM.

Small deviations of the GNR data are attributable to two main sources: the aforementioned noise amplification of our mapping procedure at long times and the dynamic error which occurs at short times [53,54], which can be empirically corrected by considering results at different camera exposure times [45]. Physically, our rod motion may deviate from the predictions of the Stokes-Einstein relation due to polymer depletion near the rod surface [5,57] or decoupling from the bulk dynamics of the polymer solution [58–61], but both effects are expected to be small in our system.

As with conventional passive microrheology [1], we used a Fourier representation of the RGSER $G^*(\omega) = [(k_BT)/(\pi s L_r^3 \mathcal{F}\{\langle\Delta\hat{u}_l^2(t)\rangle\})]$ to compute the elastic $G'(\omega)$ and loss $G''(\omega)$ moduli, where $\mathcal{F}\{\langle\Delta\hat{u}_l^2(t)\rangle\}$ is the unilateral Fourier transform of the unbounded MSAD [1]. The elastic and shear moduli of the two PEO solutions obtained from single GNR rotational nanorheology are shown in Figs. 3(e) and 3(f) by open symbols, compared to literature measurements based on diffusive wave spectroscopy [1], shown by lines. In both samples, the maximum frequency at which we can probe the viscoelasticity is limited by the maximum recording speed and the minimum exposure time of the camera, while the minimum frequency is set by the MSAD reaching its asymptote. Notably, considering the size of the measurement uncertainties we have obtained with 100 nm GNRs, the maximum modulus that can be measured by rotational nanorheology, $G^*_{\max} \approx [(K_BT)/(l^3\Delta u^2_{\min})]$, is 2 orders of magnitude larger than measurable using translational microrheology, $G^*_{\max} \approx [(K_BT)/(l\Delta r^2_{\min})]$.

The anisotropic translational Brownian motion of the GNR can be characterized by two drag coefficients parallel and perpendicular to its long axis. Following the analysis of Han *et al.* [37], in the moving body frame of the rod, translational displacements, as shown in Fig. 4(a), have a Gaussian distribution, and the corresponding MSDs in a viscous fluid, as plotted in Fig. 4(b), are a linear function of time $\langle\Delta r^2_{\parallel,\perp}\rangle = 2D_{\parallel,\perp}t$, with $D_\parallel$ and $D_\perp$ being diffusion coefficients parallel and perpendicular, respectively, to the major axis [Fig. 1(b)]. In a stationary lab frame initially aligned with the rod at $t = 0$, however, rotational diffusion of the GNR erases the particle alignment with the reference frame, causing translational diffusion to become isotropic

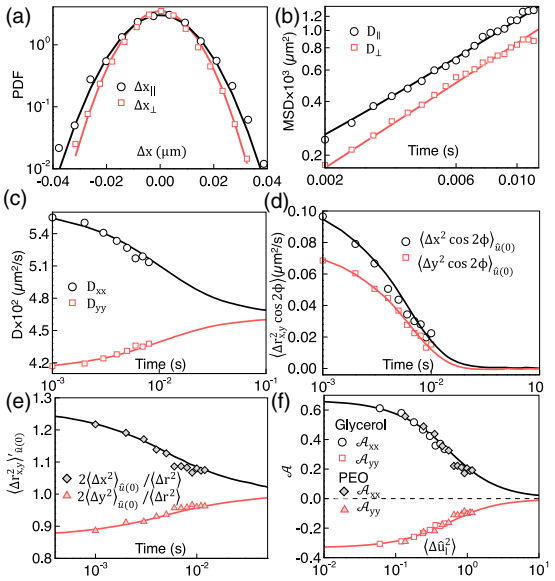

FIG. 4. Anisotropic translational displacement distributions (a), at $\tau = 2$ ms, of a GNR in 90% glycerol (symbols) with a Gaussian fit (lines) and corresponding anisotropic MSDs (b). Diffusion coefficients of the GNR (c), corresponding to the data in (a) and (b), in the fixed lab frame with the x axis aligned with the rod's initial position with the model fit [Eq. (3)]. Mixed translational and orientational correlations (d) in a fixed frame (symbols) and MC simulation (curves). Rescaled anisotropic MSDs (e) of GNR in PEO 6.7% [as in Fig. 3(e)] in the fixed lab frame (symbols) with a viscoelastic model (curves); unscaled MSDs shown in Fig. S14 [45]. Diffusion anisotropy (f), $\mathcal{A}_{ii} = (D_{ii} - D_t)/\Delta D$, for a GNR in glycerol and 6.7% PEO solution (symbols), with the model [Eq. (4)] (curves).

[37] for $\tau > \tau_\theta = 1/2D_r$. To capture this effect, we decomposed the MSDs of single GNRs into x and y directions with the initial orientation aligned in the x direction, $\langle\Delta r^2_{x,y}\rangle_{\hat{u}(0)=\hat{e}_x}$; results are shown in Fig. 4(c). As expected initially, $D_{xx}(t < \tau_\theta)$ equals to $D_\parallel$, and $D_{yy}(t < \tau_\theta)$ equals to $D_\perp$, before asymptotically approaching $D_t = (D_\parallel + 2D_\perp)/3$ at long times.

To describe such an anisotropic-to-isotropic crossover of the diffusion of uniaxial particles, we generalized the Perrin-Lubensky model [37,38] to three-dimensional rotation [45]. For a rod diffusing in a viscous fluid in 3D, we obtain

$$D_{ii} = \frac{\langle\Delta r_i^2\rangle_{\hat{u}(0)}}{2t} = D_t + \Delta D\left(u_i^2(0) - \frac{1}{3}\right)\frac{\tau}{t}, \qquad (3)$$

where $\Delta D = D_\parallel - D_\perp$ and $\tau = [1 - \exp(-6D_r t)]/6D_r$, in excellent agreement with the data [Fig. 4(c)]. For an anisotropic particle such as the GNR, the functional dependence of the translational drag coefficients on its orientation mixes correlation between translational and orientational degrees of freedom [37]. For example, we measured two cross terms $\langle\Delta x^2\cos 2\phi\rangle_{\hat{u}(0)=\hat{e}_x}$ and $\langle\Delta y^2\cos 2\phi\rangle_{\hat{u}(0)=\hat{e}_x}$,

shown by open symbols in Fig. 4(d), which agree well with the numerical result of MC simulation. We note that this apparent correlation is different from a true cross-coupling of rotational and translational diffusion, which is manifested only with chiral tracers.

Unlike viscous fluids, for viscoelastic materials such as the PEO solution, the mobility tensor of the GNR is a function of both the lag time and the orientation [45], altering the form of the anisotropic-to-isotropic crossover. We extended our model to an arbitrary nonchiral particle in a linear viscoelastic material [45]. As before, we decomposed the MSDs in x and y directions with the initial orientation of $\hat{u}(0) = \hat{e}_x$, for GNRs in viscoelastic PEO solutions [symbols in Fig. 4(e)]. Since the diffusion coefficient is not a constant, we normalized the anisotropic MSDs by their azimuthally averaged values as a function of the lag time. To model these data, we used the creep compliance J of the solution calculated from nanorheology data via $\langle \Delta \hat{u}_l(t)^2 \rangle = 2k_B T L_r^3 J(t)$. While our general model [solid lines in Fig. 4(e)] matches quantitatively with the current measurement, approximations in our approach will fail in the limit of very soft, predominantly elastic materials [45]. Equation (3) and Figs. 4(c) and 4(e) indicate that the rotational diffusion of the GNR controls the rate of the anisotropic-to-isotropic crossover. Therefore, intuitively, one should expect a universal curve for the crossover when plotted against the orientational displacement instead of the time. Figure 4(f) shows such a rescaled diffusion anisotropy defined as $\mathcal{A}_{ii} = (D_{ii} - D_t)/\Delta D$ based on MSAD for the GNR in both glycerol and PEO solutions. The data for both glycerol (open symbols) and PEO (solid symbols) collapse upon each other and the theoretical model

$$\mathcal{A}_{ii} = \left(u_i^2(0) - \frac{1}{3} \right) \frac{1 - \exp(-3\langle \Delta \hat{u}_l(t)^2 \rangle)}{3\langle \Delta \hat{u}_l(t)^{2,} \rangle}, \qquad (4)$$

plotted by solid lines.

Here we have demonstrated that tracking the rotational Brownian motion of nanorods expands the capabilities of passive microrheology to much smaller length scales and stiffer materials. Moreover, particle heating limits allow much stronger laser illumination than we use here, suggesting that smaller GNRs, stiffer materials, and higher frequencies should be accessible. We can imagine mapping out the structure and rheology at the 100 nm scale, resolving a typical bacterium into thousands of subvolumes. The small size of GNRs will also allow the probing of many interfacial systems and soft materials at or near their intrinsic length scales, such as many semiflexible polymer materials at their mesh size or lipid bilayers at the length scale of their thermal undulations. This approach promises access to nanoscale structure, dynamics, and mechanics in a wide variety of biophysical and soft material systems that are currently accessible, if at all, only to state of the art inelastic neutron or dynamics x-ray scattering methods.

This work was supported by Grant No. 55120-NDS from the ACS Petroleum Research Fund, with partial support from the Penn PSOC program, NIH U54-CA193417. We acknowledge useful conversations with Robert Leheny, Eric Weeks, and Tom Lubensky.

*Corresponding author.
jcrocker@seas.upenn.edu

[1] B. R. Dasgupta, S.-Y. Tee, J. C. Crocker, B. J. Frisken, and D. A. Weitz, Microrheology of polyethylene oxide using diffusing wave spectroscopy and single scattering, Phys. Rev. E **65**, 051505 (2002).
[2] T. G. Mason, Estimating the viscoelastic moduli of complex fluids using the generalized Stokes–Einstein equation, Rheol. Acta **39**, 371 (2000).
[3] T. G. Mason, K. Ganesan, J. H. Van Zanten, D. Wirtz, and S. C. Kuo, Particle Tracking Microrheology of Complex Fluids, Phys. Rev. Lett. **79**, 3282 (1997).
[4] T. G. Mason and D. A. Weitz, Optical Measurements of Frequency-Dependent Linear Viscoelastic Moduli of Complex Fluids, Phys. Rev. Lett. **74**, 1250 (1995).
[5] D. T. Chen, E. R. Weeks, J. C. Crocker, M. F. Islam, R. Verma, J. Gruber, A. J. Levine, T. C. Lubensky, and A. G. Yodh, Rheological Microscopy: Local Mechanical Properties from Microrheology, Phys. Rev. Lett. **90**, 108301 (2003).
[6] J. C. Crocker, M. T. Valentine, E. R. Weeks, T. Gisler, P. D. Kaplan, A. G. Yodh, and D. A. Weitz, Two-point microrheology of inhomogeneous soft materials, Phys. Rev. Lett. **85**, 888 (2000).
[7] M. L. Gardel, M. T. Valentine, J. C. Crocker, A. R. Bausch, and D. A. Weitz, Microrheology of Entangled F-actin Solutions, Phys. Rev. Lett. **91**, 158302 (2003).
[8] A. W. C. Lau, B. D. Hoffman, A. Davies, J. C. Crocker, and T. C. Lubensky, Microrheology, Stress Fluctuations, and Active Behavior of Living Cells, Phys. Rev. Lett. **91**, 198101 (2003).
[9] K. He, F. Babaye Khorasani, S. T. Retterer, D. K. Thomas, J. C. Conrad, and R. Krishnamoorti, Diffusive Dynamics of Nanoparticles in Arrays of Nanoposts, ACS Nano **7**, 5122 (2013).
[10] T. M. Squires and T. G. Mason, Fluid mechanics of microrheology, Annu. Rev. Fluid Mech. **42**, 413 (2010).
[11] Z. Cheng and T. G. Mason, Rotational Diffusion Microrheology, Phys. Rev. Lett. **90**, 018304 (2003).
[12] E. Andablo-Reyes, P. Díaz-Leyva, and J. L. Arauz-Lara, Microrheology from Rotational Diffusion of Colloidal Particles, Phys. Rev. Lett. **94**, 106001 (2005).
[13] C. Haro-Pérez, E. Andablo-Reyes, P. Díaz-Leyva, and J. L. Arauz-Lara, Microrheology of viscoelastic fluids containing light-scattering inclusions, Phys. Rev. E **75**, 041505 (2007).
[14] F. C. Cheong and D. G. Grier, Rotational and translational diffusion of copper oxide nanorods measured with holographic video microscopy, Opt. Express **18**, 6555 (2010).
[15] K. V. Edmond, M. T. Elsesser, G. L. Hunter, D. J. Pine, and E. R. Weeks, Decoupling of rotational and translational diffusion in supercooled colloidal fluids, Proc. Natl. Acad. Sci. U.S.A. **109**, 17891 (2012).

[16] G. L. Hunter, K. V. Edmond, M. T. Elsesser, and E. R. Weeks, Tracking rotational diffusion of colloidal clusters, Opt. Express **19**, 17189 (2011).
[17] D. Mukhija and M. J. Solomon, Translational and rotational dynamics of colloidal rods by direct visualization with confocal microscopy, J. Colloid Interface Sci. **314**, 98 (2007).
[18] A. Wang, T. G. Dimiduk, J. Fung, S. Razavi, I. Kretzschmar, K. Chaudhary, and V. N. Manoharan, Using the discrete dipole approximation and holographic microscopy to measure rotational dynamics of non-spherical colloidal particles, J. Quant. Spectrosc. Radiat. Transfer **146**, 499 (2014).
[19] X. Cheng, X. Cao, B. Xiong, Y. He, and E. S. Yeung, Background-free three-dimensional selective imaging of anisotropic plasmonic nanoparticles, Nano Res. **10**, 1423 (2017).
[20] K. Marchuk and N. Fang, Three-dimensional orientation determination of stationary anisotropic nanoparticles with sub-degree precision under total internal reflection scattering microscopy, Nano Lett. **13**, 5414 (2013).
[21] K. Marchuk, J. W. Ha, and N. Fang, Three-dimensional high-resolution rotational tracking with superlocalization reveals conformations of surface-bound anisotropic nanoparticles, Nano Lett. **13**, 1245 (2013).
[22] C. Sönnichsen and A. P. Alivisatos, Gold nanorods as novel nonbleaching plasmon-based orientation sensors for polarized single-particle microscopy, Nano Lett. **5**, 301 (2005).
[23] E. J. Titus and K. A. Willets, Accuracy of superlocalization imaging using gaussian and dipole emission point-spread functions for modeling gold nanorod luminescence, ACS Nano **7**, 6258 (2013).
[24] G. Wang, W. Sun, Y. Luo, and N. Fang, Resolving rotational motions of nano-objects in engineered environments and live cells with gold nanorods and differential interference contrast microscopy, J. Am. Chem. Soc. **132**, 16417 (2010).
[25] A. J. Wilson and K. A. Willets, Surface-enhanced Raman scattering imaging using noble metal nanoparticles, Wiley Interdiscip. Rev.: Nanomed. Nanobiotechnol. **5**, 180 (2013).
[26] L. Xiao, Y. Qiao, Y. He, and E. S. Yeung, Three dimensional orientational imaging of nanoparticles with darkfield microscopy, Anal. Chem. **82**, 5268 (2010).
[27] L. Xiao, Y. Qiao, Y. He, and E. S. Yeung, Imaging translational and rotational diffusion of single anisotropic nanoparticles with planar illumination microscopy, J. Am. Chem. Soc. **133**, 10638 (2011).
[28] L. Xiao, L. Wei, C. Liu, Y. He, and E. S. Yeung, Unsynchronized translational and rotational diffusion of nanocargo on a living cell membrane, Angew. Chem., Int. Ed. **51**, 4181 (2012).
[29] L. Xiao and E. S. Yeung, Optical imaging of individual plasmonic nanoparticles in biological samples, Annu. Rev. Anal. Chem. **7**, 89 (2014).
[30] D. Xu, Y. He, and E. S. Yeung, Direct imaging of transmembrane dynamics of single nanoparticles with darkfield microscopy: improved orientation tracking at cell sidewall, Anal. Chem. **86**, 3397 (2014).
[31] H. Yuan, S. Khatua, P. Zijlstra, and M. Orrit, Individual gold nanorods report on dynamical heterogeneity in supercooled glycerol, Faraday Discuss. **167**, 515 (2013).
[32] S. Alam and A. Mukhopadhyay, Translational and rotational diffusions of nanorods within semidilute and entangled polymer solutions, Macromolecules **47**, 6919 (2014).
[33] S. Alam and A. Mukhopadhyay, Translational anisotropy and rotational diffusion of gold nanorods in colloidal sphere solutions, Langmuir **31**, 8780 (2015).
[34] R. K. Chhetri, R. L. Blackmon, W.-C. Wu, D. B. Hill, B. Button, P. Casbas-Hernandez, M. A. Troester, J. B. Tracy, and A. L. Oldenburg, Probing biological nanotopology via diffusion of weakly constrained plasmonic nanorods with optical coherence tomography, Proc. Natl. Acad. Sci. U.S.A. **111**, E4289 (2014).
[35] R. K. Chhetri, K. A. Kozek, A. C. Johnston-Peck, J. B. Tracy, and A. L. Oldenburg, Imaging three-dimensional rotational diffusion of plasmon resonant gold nanorods using polarization-sensitive optical coherence tomography, Phys. Rev. E **83**, 040903 (2011).
[36] R. K. Chhetri and A. L. Oldenburg, in *Frontiers in Optics* (Optical Society of America, Washington, DC, 2012), p. FTu4E. 3.
[37] Y. Han, A. M. Alsayed, M. Nobili, J. Zhang, T. C. Lubensky, and A. G. Yodh, Brownian motion of an ellipsoid, Science **314**, 626 (2006).
[38] F. Perrin, Mouvement Brownien d'un ellipsoide (II). Rotation libre et dépolarisation des fluorescences. Translation et diffusion de molécules ellipsoidales, J. Phys. Radium **7**, 1 (1936).
[39] S. Link and M. A. El-Sayed, Spectral properties and relaxation dynamics of surface plasmon electronic oscillations in gold and silver nanodots and nanorods, J. Phys. Chem. B **103**, 8410 (1999).
[40] C. F. Bohren and D. R. Huffman, *Absorption and Scattering of Light by Small Particles* (John Wiley & Sons, New York, 1983), p. 82.
[41] A. Brioude, X. Jiang, and M. Pileni, Optical properties of gold nanorods: DDA simulations supported by experiments, J. Phys. Chem. B **109**, 13138 (2005).
[42] P. K. Jain, S. Eustis, and M. A. El-Sayed, Plasmon coupling in nanorod assemblies: optical absorption, discrete dipole approximation simulation, and exciton-coupling model, J. Phys. Chem. B **110**, 18243 (2006).
[43] E. M. Purcell and C. R. Pennypacker, Scattering and absorption of light by nonspherical dielectric grains, Astrophys. J. **186**, 705 (1973).
[44] M. A. Yurkin and A. G. Hoekstra, The discrete-dipole-approximation code ADDA: capabilities and known limitations, J. Quant. Spectrosc. Radiat. Transfer **112**, 2234 (2011).
[45] See Supplemental Material at http://link.aps.org/supplemental/10.1103/PhysRevLett.120.118002 for additional details about the experimental setup, sample preparation, simulations, and derivation, which includes Refs. [46–52].
[46] D. Axelrod, Carbocyanine dye orientation in red cell membrane studied by microscopic fluorescence polarization, Biophys. J. **26**, 557 (1979).
[47] H. J. Chen, L. Shao, Q. Li, and J. F. Wang, Gold nanorods and their plasmonic properties, Chem. Soc. Rev. **42**, 2679 (2013).
[48] P. B. Johnson and R. W. Christy, Optical constants of the noble metals, Phys. Rev. B **6**, 4370 (1972).

[49] M. Khan and T. G. Mason, Trajectories of probe spheres in generalized linear viscoelastic complex fluids, Soft Matter **10**, 9073 (2014).
[50] M. Khan and T. G. Mason, Random walks of colloidal probes in viscoelastic materials, Phys. Rev. E **89**, 042309 (2014).
[51] I. Teraoka, *Front Matter and Index* (Wiley Online Library, New York, 2002).
[52] M. Rubinstein and R. H. Colby, *Polymer Physics* (Oxford University, New York, 2003), Vol. 23.
[53] J. C. Crocker and D. G. Grier, Methods of digital video microscopy for colloidal studies, J. Colloid Interface Sci. **179**, 298 (1996).
[54] T. Savin and P. S. Doyle, Static and dynamic errors in particle tracking microrheology, Biophys. J. **88**, 623 (2005).
[55] I. Martchenko, H. Dietsch, C. Moitzi, and P. Schurtenberger, Hydrodynamic properties of magnetic nanoparticles with tunable shape anisotropy: prediction and experimental verification, J. Phys. Chem. B **115**, 14838 (2011).
[56] M. M. Tirado, C. L. Martínez, and J. G. de la Torre, Comparison of theories for the translational and rotational diffusion coefficients of rod-like macromolecules. Application to short DNA fragments, J. Chem. Phys. **81**, 2047 (1984).
[57] A. J. Levine and T. C. Lubensky, One-and Two-Particle Microrheology, Phys. Rev. Lett. **85**, 1774 (2000).
[58] L.-H. Cai, S. Panyukov, and M. Rubinstein, Mobility of nonsticky nanoparticles in polymer liquids, Macromolecules **44**, 7853 (2011).
[59] Y. Cheng, R. K. Prud'Homme, and J. L. Thomas, Diffusion of mesoscopic probes in aqueous polymer solutions measured by fluorescence recovery after photobleaching, Macromolecules **35**, 8111 (2002).
[60] I. Kohli and A. Mukhopadhyay, Diffusion of nanoparticles in semidilute polymer solutions: effect of different length scales, Macromolecules **45**, 6143 (2012).
[61] R. Poling-Skutvik, R. Krishnamoorti, and J. C. Conrad, Size-dependent dynamics of nanoparticles in unentangled polyelectrolyte solutions, ACS Macro Lett. **4**, 1169 (2015).